



Strain rate effects on fragment morphology of ceramic alumina: A synchrotron-based study

J.Y. Huang^a, C.K. Lin^a, Y.L. Bian^c, H.L. Xie^d, H.W. Chai^{b,*}, Y.Y. Ding^{a,*}, S.N. Luo^b

^a MOE Key Laboratory of Impact and Safety Engineering, Ningbo University, Ningbo, Zhejiang, PR China

^b School of Materials Science and Engineering, Southwest Jiaotong University, Chengdu, Sichuan, PR China

^c The Peac Institute of Multiscale Sciences, Chengdu, Sichuan, PR China

^d Shanghai Institute of Applied Physics, Chinese Academy of Sciences, Shanghai, PR China



ARTICLE INFO

Keywords:

Alumina ceramic
Dynamic compression
Synchrotron computed tomography
Fragment morphology
Fracture modes

ABSTRACT

Dynamic ($600\text{--}1000\text{ s}^{-1}$) and quasi-static ($0.001\text{--}0.01\text{ s}^{-1}$) compression experiments are conducted on a high-purity alumina ceramic using a split Hopkinson pressure bar and a material test system, respectively. The postmortem fragments of ceramic samples at different strain rates are then characterized via synchrotron micro computed tomography (CT). The three-dimensional (3D) morphologies of fragments are quantified using the gyration tensor analysis after proper segmentation of CT images. The mean fragment size decreases in a power-law form while the mean shape indices (sphericity, elongation index and flatness index) increase in a logarithmic-linear form, with increasing strain rates. In addition, the fragment size and shape distributions are all found to follow the Weibull probability distribution. To reveal the underlying mechanisms of such strain rate effects, high-speed optical and X-ray imaging are implemented to capture the fracture process of ceramic samples under quasi-static and dynamic compression. Primary and secondary wing cracks (PWCs/SWCs) control the fracture and fragmentation of the ceramic under both loading conditions. Compared to quasi-static loading, a considerably larger number of SWCs are produced under dynamic loading, and pronounced branching and bridging occur among the PWCs, which prevent the PWCs from coalescing into axial splitting cracks. Consequently, crack networks composed of high-density wing cracks break the sample into finer and more isotropic fragments, consistent with CT characterizations. Scanning electron microscopy is utilized to analyze the micro damage modes of ceramic samples. Transgranular fracture dominates the grain-scale damage and contributes to the higher dynamic fracture resistance of the alumina under dynamic loading, as a result of more homogeneous nucleation and growth of micro cracks.

1. Introduction

Ceramic materials exhibit excellent mechanical properties [1–3] including low density, high hardness and high compressive strength, and have been widely used as layered armour in defense industries [4–8]. Alumina or Al_2O_3 ceramics have attracted special attention due to its good sintering performance and stable product size [9]. Al_2O_3 ceramics can provide good defense capability at a relatively low cost [4,10] and is broadly applied to composite armor of vehicles, aircrafts and soldiers [11,12], which inevitably undergo ballistic impacts during service. Therefore, the impact fragmentation of Al_2O_3 ceramics is critical for safety evaluation and structural design optimization of ceramic armours [13–15]. However, compared to the widely-discussed fracture strengths [2,16–21] and ballistic properties [13,22,23], the fragmentation morphologies (especially in three-dimensions (3D)) of ceramics under high strain rate loading have been rarely touched [24].

Compaction of damaged or fragmented ceramics affects the penetration resistance of intruders [12,25]. The compaction response of fragments depends highly on their size, shape and surface roughness [26,27]. Therefore, 3D morphologies of fragments are important for understanding fracture mechanisms of ceramic armours during foreign object penetration, and accurate numerical modeling of ballistic processes in general [7,19,23]. In addition, 50%–70% personnel trauma comes from secondary injury caused by explosive debris [28,29]. The morphologies of debris particles are useful for diagnosis and cure of blast injury, as well as evaluation of weapon/armour performance. Therefore, ceramic armours in service experience a wide range of strain rates spanning from 10^{-3} s^{-1} to 10^4 s^{-1} . Effects of strain rate on fragment morphologies of ceramics are significant for optimizing armour design. In this regard, a large number of studies were devoted to the fragmentation of brittle materials including

* Corresponding authors.

E-mail addresses: hwchai@pims.ac.cn (H.W. Chai), dingyuanyuan@nbu.edu.cn (Y.Y. Ding).

Nomenclature	
2D	Two-dimensional or two-dimension
3D	Three-dimensional or three-dimension
CCD	Charge coupled device
CT	Computed tomography
EI	Elongation index
G-C	Glenn–Chudnovsky
HCP	Hexagonal-close-packed
MTS	Material test system
PCI	Phase contrast imaging
PWC	Primary wing cracks
SEM	Scanning electron microscopy
SHPB	Split Hopkinson pressure bar
SSRF	Shanghai Synchrotron Facility
SWC	Secondary wing cracks
XRD	X-ray diffraction
A_b	Cross-sectional area of bar
A_s	Cross-sectional area of sample
C_b	Wave velocity of bar
C	Longitudinal wave velocity
c	Strain-rate sensitivity coefficient
E_b	Young's modulus of bar
E	Elastic modulus of alumina
f	Number frequency
f_0	Weibull amplitude parameter
G_c	Fracture energy
\mathbf{G}	Gyration tensor
k	Weibull shape parameter
L_s	Sample length
N_V	Number of voxels occupied
p_0	Quasi-static fragment size limit
p_1	Fitting parameter
$r_{\alpha i}^{(m)}, r_{\beta i}^{(m)}$	Coordinates of a voxel i of fragment m
$r_\alpha^{(b)} (r_\beta^{(b)})$	Coordinates of the barycentre of fragment m
R_1, R_2, R_3	Eigenvalues of the gyration tensor
$\vec{R}_1, \vec{R}_2, \vec{R}_3$	Eigenvectors of the gyration tensor
s	Fragment size
s_0	Characteristic fragment size
\bar{s}	Normalized fragment size
S_G	Sphericity
V_m	Volume of fragment m
X	Physical variables under consideration
x, y, z	Coordinate axes
Y	Physical variables under consideration
Y_r	Reference value of Y
α, β	Subscripts, corresponding to the x, y, z -axes
Γ	Γ function
ε_i	Strain of the incident bar
$\dot{\varepsilon}_r$	Reference strain rate
ε_t	Strain of the transmission bar
$\dot{\varepsilon}$	Strain rate
$\dot{\varepsilon}_0$	Characteristic strain rate
$\bar{\varepsilon}$	Normalized strain rate
$\dot{\varepsilon}_{\text{eng}}$	Engineering strain rate
$\dot{\varepsilon}_n$	Normalization factor for strain rate
λ	Weibull scale parameter
σ_{eng}	Engineering stress
σ_c	Compressive strength
σ_0	Characteristic compressive strength
σ_t	Tensile strength

the aspect ratio of fragments of B_4C ceramic [24] and monocrystalline silicon [35] after dynamic crushing was quantified via two-dimensional (2D) imaging processing, but the 2D characterizations cannot describe the volume characteristics of fragments. 3D characterizations like laboratory computed tomography (CT) have been used to explore the debris morphologies of a glass-bead chain under impact [36]. However, the debris particles below 40 μm cannot be resolved due to its limited spatial resolution (17.66 μm), and the particle shapes were not discussed either.

From a broader perspective, laboratory CT has also been applied to the morphology analysis of geological particles (soil and rock aggregates) [37–39] and powder particles [40,41]. A series of shape indices, such as sphericity, roundness, convexity, and elongation/flatness index (similar to the aspect ratio in 2D), have been proposed based on the 3D images, and used for morphology quantification of ceramic fragments. Nevertheless, most of these indices were defined in terms of the surface profiles of particles, using a minimal bounding box [38] or principal component analysis [42]. Such indices in nature are sensitive to the surface roughness and may not fully describe the volume features of particles (especially porous particles), as argued in previous studies [43]. In addition, there are different ways of defining the minimal bounding box, leading to ambiguity about the definition of particle dimensions [44].

In recent years, synchrotron-based micro CT has been developed to characterize the 3D morphology of particles [43,45], pores [45–48] and cracks [43,49–51]. Synchrotron sources produce X-rays with high brilliance, high coherence and high repetition rate, in which phase contrast imaging (PCI) can be implemented during CT scan. Synchrotron micro CT facilitates characterization of a massive number of particles or fragments at the micron scale ($\sim 3 \mu\text{m}$ [47]), and provides sufficient statistical significance for subsequent morphology analyses. In addition, edge enhancement via phase contrast benefits segmentation and extraction of 3D surfaces of particles (especially low-density particles) [39,40,43]. Combined with proper segmentation and topological analysis [40,43,52], the 3D shape parameters of fragments can be quantified using the gyration tensor analysis [43,46,53]. The gyration-tensor-based shape indices describe the rotational symmetry of particles and are less sensitive to the surface roughness of them. They fully take into account the 3D information of fragments and are more appropriate for quantifying the 3D morphologies of particles. Previous studies [17,54] showed that strain rate imposed significant influence on cracking dynamics and thus fragment morphologies of ceramic materials. Scaling laws between the fragment size/shape and strain rate can improve our understanding of the fracture and energy dissipation mechanisms [25], and supply critical constraints on the constitutive or numerical modeling of ceramics under ballistic impact [7,12]. Nevertheless, 3D characterizations on the fragment morphologies of entire ceramic samples using synchrotron CT have not been reported yet; the strain rate effects on the fragment size/shapes of ceramics along with the underlying mechanisms remain to be interesting but open questions.

ceramics under various loading rates [18,30–33]. Several theoretical models [30–32] were developed for predicting the mean fragment sizes under different loading rates, and agree well with the experimental measurements. In the experiment, photography and laser interferometry were used to measure the fragment size distributions of ceramics (e.g., Al_2O_3 [18], B_4C [24,34]) after dynamic compression. In addition,

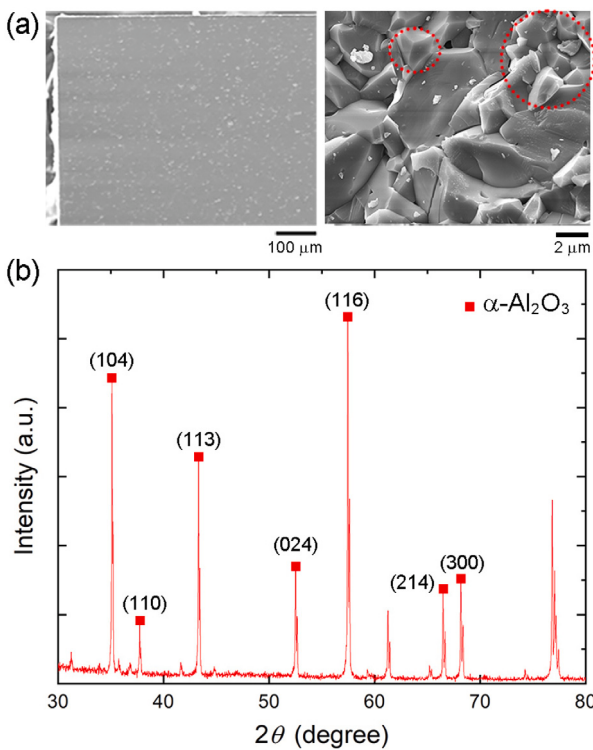


Fig. 1. Initial characterizations of the alumina ceramic. (a) Scanning electron microscopy (SEM) images of an intact (left) and a fractured (right) sample surface, which show basically intact sample edges and an equiaxed grain structure, respectively. (b) X-ray diffraction (XRD) pattern acquired with a Cu-K α source. The main peaks of the $\alpha\text{-Al}_2\text{O}_3$ phase are marked.

This study aims to investigate the strain rate effects on the 3D fragment morphology (particularly shape) of ceramic alumina using various techniques. For clarity, a flowchart of the technical routes and corresponding facilities used is presented in Fig. A.1. A high-purity alumina is compressed to fracture under quasi-static ($0.001\text{--}0.01\text{ s}^{-1}$) and dynamic ($600\text{--}1000\text{ s}^{-1}$) loading with a material testing system (MTS) and a split Hopkinson pressure bar (SHPB), respectively. Then the ceramic fragments formed under different strain rates are characterized with synchrotron micro CT at the Shanghai Synchrotron Facility (SSRF) [45,51,55]. Statistical analyses are conducted on fragment morphology using the gyration tensor analysis. Strain rate has a pronounced effect on fragment shape: the fragments under dynamic loading appear finer and more isotropic. The underlying mechanisms for the strain rate effects are examined with high-speed optical/X-ray imaging along with scanning electron microscopy.

2. Materials and methods

In this section, the material and methodology used in this work are presented in Sections 2.1 and 2.2, respectively. The setups and procedures of the SHPB loading and CT characterization experiments are described in detail, while the MTS tests and routine characterizations such as X-ray diffraction (XRD) and scanning electron microscopy (SEM) are briefly mentioned.

2.1. Materials and initial characterizations

The experimental material is an Al_2O_3 ceramic prepared by Shanghai Daheng Optical Precision Machinery Co., Ltd. by tape casting. The initial density of the Al_2O_3 ceramic measured by an analytical balance is 3.74 g cm^{-3} , about 96% of the full density of Al_2O_3 . Considering that thin ceramic plates are used in composite armour, plate-shaped samples

are adopted for compression experiments. The as-cast plate (1-mm thick) is ground, polished, and then manufactured into experimental samples via diamond cutting and polishing. The sample dimensions are $3 \times 3 \times 1\text{ mm}^3$. Small samples facilitates rapid stress equilibrium under high strain rate loading. A moderate number of fragments is also beneficial to postmortem CT characterizations.

Initial characterizations are then conducted on the Al_2O_3 ceramic sample with SEM and XRD. The SEM characterization is performed using the SU5000 scanning electron microscope (Hitachi, Japan). XRD is performed using the SmartLab SE diffractometer (Rigaku, Japan). A copper anode operating at 40 kV and 40 mA yields Cu-K α radiation with a wavelength of 0.15405 nm . The diffraction angle (2θ) varies from 30° to 80° . The SEM image of a sample prior to loading (left column, Fig. 1a) confirms that the edges of the sample are basically intact with little cutting damage. The SEM image of a fractured surface (right column, Fig. 1a) illustrates that the Al_2O_3 ceramic has fine equiaxed grains (as marked by the dashed ellipses). The grain size is in the range of $1\text{--}5\text{ }\mu\text{m}$. The X-ray diffraction pattern (Fig. 1b) indicates that the ceramic material consists of mainly the $\alpha\text{-Al}_2\text{O}_3$ phase with a hexagonal-close-packed (HCP) crystal structure [56].

2.2. SHPB loading

The quasi-static and dynamic compression experiments are conducted with the MTS and SHPB, respectively. The schematic diagram of the SHPB implemented with high-speed optical imaging is illustrated in Fig. 2a. The striker (1), incident bar (2) and transmission bar (4) are all made of high-strength steel with a diameter 6 mm , and the lengths are 150 mm , 500 mm and 500 mm , respectively [35]. To protect the bar ends, a pair of diamond inserts of the same 6-mm diameter are sandwiched between the incident and transmission bars [2]. Vaseline is spread onto all the contact surfaces to reduce friction. Pulse shapers made of rubber are used to obtain a rising slope of the incident wave. The pulse shapes are 5 mm in diameter, and $0.5\text{--}1.5\text{ mm}$ in thickness, depending on the desired loading strain rate. A cuboidal polycarbonate box with through holes are manufactured to recover the ceramic fragments.

Upon loading, impact of the striker on the incident bar generates an elastic wave propagating through the bar (along the x -axis, Fig. 2a). When the incident wave arrives at the interface between the incident bar and the sample (3), it is partially reflected owing to impedance mismatch, while the rest is transmitted into the transmission bar. The incident wave, reflected wave and transmission wave are registered with the strain gauges (5) on the incident and transmission bars. Three-wave analysis indicates that stress uniformity is achieved long before the failure of sample. Then, the stress, strain and strain rate histories can be calculated according to the two-wave technique using the incident and transmission waves [57]. The engineering stress σ_{eng} and engineering strain rate $\dot{\epsilon}_{\text{eng}}$ are derived as follows,

$$\sigma_{\text{eng}} = E_b \epsilon_t \frac{A_b}{A_s}, \quad (1)$$

$$\dot{\epsilon}_{\text{eng}} = \frac{2C_b (\epsilon_t - \epsilon_i)}{L_s}, \quad (2)$$

where ϵ_i and ϵ_t are strains of the incident and transmission bars. E_b and C_b are Young's modulus and wave velocity of the bar. A_b and A_s are cross-sectional areas of the bar and the specimen, respectively. L_s is sample length. Compressive stress is taken positive.

During dynamic and quasi-static loading, *in situ*, high-speed optical imaging is adopted to monitor the deformation and failure process of ceramic samples. Halogen lights are used to illuminate the sample and the imaging is conducted with the Photron FASTCAM camera in a reflection mode. The frame rate of the high-speed camera is set to 210 kHz , and the exposure time, $1\text{ }\mu\text{s}$, under both loading conditions. Under dynamic loading, the incident wave pulse is used to trigger the camera in a start trigger mode. Then the whole deformation and

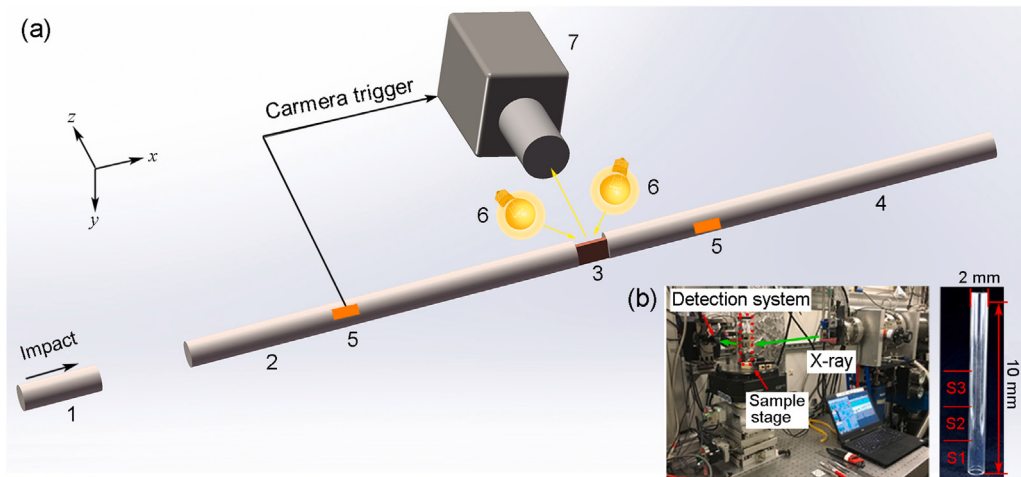


Fig. 2. Experimental setups for dynamic compression and synchrotron X-ray computed tomography (CT). (a) Schematic diagram of the split Hopkinson pressure bar implemented with high-speed optical imaging. 1: striker; 2: incident bar; 3: sample; 4: transmission bar; 5: strain gauges; 6: flash lights; 7: high-speed camera. Impact direction: x axis. (b) Pictures of the CT system (left) at the Shanghai Synchrotron Facility (SSRF), and the sample holder (right) used. The CT system mainly consists of the X-ray source (green arrows), sample stage and detection system. Three scans (marked as S1–S3) are performed along the sample height direction to cover all the fragments of each sample.

fracture process of the sample is recorded. However, the recording time of the camera is far shorter than the loading time under quasi-static loading, and hence only the fracture process around the peak stress is recorded. In this case, the stress unloading signal owing to catastrophic failure of the sample is used to trigger the camera in an end trigger mode. The images of the sample before the trigger point are captured. In addition, *in situ*, high-speed X-ray imaging is utilized to capture the internal dynamic fracture process. The high-speed X-ray imaging experiments are also conducted in SSRF. The frame rate of the high-speed camera is set to 100 kHz, and the exposure time, 3 μ s. More details on the SHPB-based high-speed X-ray imaging were documented elsewhere [35,58–60].

2.3. CT characterizations

3D characterizations of the recovered fragments is conducted by synchrotron CT. A photograph of the CT setup is shown in Fig. 2b (the left column), including the X-ray source, sample stage and X-ray detection system. The fragments are collected in a poly(methylmethacrylate) tube for CT scan (Fig. 2b, right column). Three scans (marked as S1–S3) are performed along the sample height direction to cover the whole fragments of each sample. The X-ray energy is selected as 24.9 keV. Incident X-rays penetrate the sample, are converted into visible light via scintillators (60 mm away from the sample), and are imaged on a charge coupled device (CCD) camera. The CCD has 2560×2000 pixels, and the pixel size is 0.87 μ m. 1500 projections are evenly collected within 180° in one scan. Then, the projections are reconstructed into 3D images with the software PITRE [61]. The spatial resolution of the 3D images is estimated using the Fourier domain method [62], and is about 3 μ m.

The reconstructed volume data are processed to identify and quantify the morphologies of fragments and residual internal cracks using the Avizo software. The detailed processing steps are basically the same with those illustrated in our previous publication [43], and only the key points are repeated here for brevity. Firstly, the solid phase (fragments) and the air phase are segmented via thresholding segmentation, and then the two phases are eroded by 3–5 pixels. Secondly, the marker-controlled watershed algorithm [63] is applied to the eroded image to identify the surface profiles of the fragments, using the “watershed tool” module in Avizo. Thirdly, the classic watershed algorithm [64] is adopted to separate contacts between different fragments. A loose packing of the fragments yields a simple contact geometry beneficial for contact segmentation. Nevertheless, contact partitioning is visually

inspected to repair unsegmented or over-segmented fragments. Then the volume data of all fragments are obtained and directly used for morphological calculation through the gyration tensor analysis (see details in Section 3.2). Finally, residual cracks inside the fragments are also extracted. A closing operation is performed on the segmented image of fragments and air phase, followed by visual inspection to repair unclosed areas. The crack phase (part of the air phase) is extracted by subtracting the image before closing from the obtained image.

3. Results and discussions

In this section, the experimental results and corresponding discussions are presented in five subsections. Specifically, the ceramic samples are firstly compressed to fracture at four strain rates (0.001 s^{-1} , 0.01 s^{-1} , 600 s^{-1} , 1000 s^{-1}). The fracture strengths at different strain rates are presented and discussed in Section 3.1. Then, the fragments of ceramic samples are recovered for CT scan. The size and shape index distributions of fragments are quantified for each strain rate, and the strain rate effects on the fragment morphology are discussed in Section 3.2. To clarify the intrinsic mechanisms for strain rate effects, high-speed optical/X-ray imaging, and postmortem SEM characterizations are carried out, and the results are presented in Sections 3.3 and 3.4, respectively, along with a brief discussion in Section 3.5.

3.1. Fracture strengths

The fracture strengths of ceramic samples under different strain rates are summarized in Fig. 3, along with the data of a similar alumina from Ref. [17]. The mean fracture strengths under quasi-static loading (0.001 s^{-1} and 0.01 s^{-1}) are obtained by averaging over 10 repeat tests, and error bars represent the standard deviations. At least three repeat tests are carried out for each dynamic strain rate, and the fracture strengths from all dynamic tests are presented. For clarity, the range of strain rates for quasi-static and dynamic loading is roughly marked in the figure. The quasi-static and dynamic strength data both exhibit certain scatter as a result of random nucleation of damage around initial defects [33]. With increasing strain rates, the compressive strength of the Al_2O_3 ceramic remains approximately constant before a critical strain rate (around 500 s^{-1} , as illustrated in Fig. 3), but increases sharply after that, consistent with the previous results [17,65]. The enhanced strain-rate sensitivity under high strain rate loading is mainly attributed to the increased crack density and

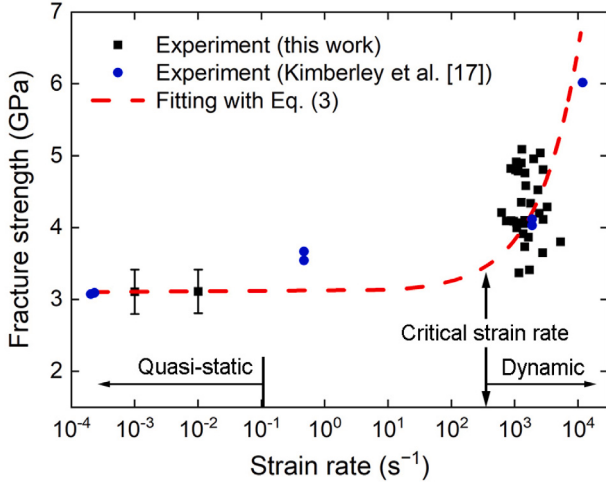


Fig. 3. Compressive fracture strength of the alumina as a function of strain rate (in the logarithmic scale). Literature data along with a power law fitting are plotted for comparison. Error bars refer to standard deviations of ten repeat measurements under quasi-static loading.

crack interactions in ceramic samples [17,66,67]. This strain rate dependence of the compressive strength (σ_c) can be described by a power law like,

$$\sigma_c = \sigma_0 \left[1 + \left(\frac{\dot{\epsilon}}{\dot{\epsilon}_n} \right)^{\frac{2}{3}} \right], \quad (3)$$

where $\dot{\epsilon}$ is strain rate. σ_0 is characteristic compressive strength when $\dot{\epsilon}$ approaches 0 (e.g., 0.001 s⁻¹), and is chosen as 3.11 GPa. $\dot{\epsilon}_n$ is normalization factor for strain rate. The experimental data is in good agreement with the theoretical model. The fitted $\dot{\epsilon}_n$ is about 8733 s⁻¹.

3.2. Morphology analysis of fragments

Fig. 4 presents the CT characterizations of the ceramic fragments at different strain rates. For visualization of the fragments, triangular surface meshes [52] are created on the segmented fragments using the “Generate Surface” module in Avizo. For brevity, only two volume renderings of the fragments at 0.001 s⁻¹ and 600 s⁻¹ (as noted) are presented in **Fig. 4a**. Pseudo color coding is applied to distinguish different fragments with diverse sizes and shapes. The fragments for the 600 s⁻¹ case are considerably finer than those for the 0.001 s⁻¹ case.

To quantify the fragment morphology in 3D, gyration tensor analysis is adopted to calculate the shape indices, including sphericity, elongation index (EI) and flatness index (FI), of fragments using the unsmoothed segmented volume data. A schematic diagram of the gyration tensor analysis is shown in **Fig. 4b**. Firstly, a gyration tensor \mathbf{G} is defined in terms of the voxels of a fragment as

$$G_{\alpha\beta} = \frac{1}{V_m} \sum_{i=1}^{N_v} \left(r_{\alpha_i}^{(m)} - r_{\alpha}^{(b)} \right) \left(r_{\beta_i}^{(m)} - r_{\beta}^{(b)} \right). \quad (4)$$

Here V_m is volume of fragment m , and N_v is number of voxels occupied by fragment m . $r_{\alpha_i}^{(m)}$ and $r_{\beta_i}^{(m)}$ are the coordinates of voxel i ($\alpha, \beta = x, y, z$), and $r_{\alpha}^{(b)}$ and $r_{\beta}^{(b)}$ are the coordinates of the barycentre (b) of fragment m , respectively. The eigenvalues of the gyration tensor are calculated as R_1 , R_2 and R_3 ($R_1 > R_2 > R_3$), along with the corresponding eigenvectors \vec{R}_1 , \vec{R}_2 and \vec{R}_3 . Then, a characteristic ellipsoid (**Fig. 4b**) can be constructed with its three semi-axes oriented along the eigenvectors, and their lengths are $\sqrt{5R_1}$, $\sqrt{5R_2}$ and $\sqrt{5R_3}$, respectively. This characteristic ellipsoid is only for the illustrative purpose, and does not

affect the definitions of shape indices. The sphericity index S_G can be defined with the eigenvalues as

$$S_G = 1 - \frac{1}{2} \frac{\sum_{i>j}^3 (R_i - R_j)^2}{\left(\sum_i^3 R_i \right)^2}. \quad (5)$$

Higher S_G indicates more spherical fragments. The FI and EI are defined as

$$FI = R_3/R_2; \quad EI = R_2/R_1. \quad (6)$$

Lower FI or EI indicates flatter or more elongated fragments, respectively.

The cumulative size, sphericity, EI and FI distributions of the fragments under different strain rates are presented in **Fig. 4c-f**. Each curve represents the average over three repeat (CT) measurements, with error bars denoting the standard deviations. The size and shape index distributions of the fragments show obvious scatter (large error bars), and spans in a wide range under both dynamic and quasi-static loading. With increasing strain rates, the size distribution curves shift toward smaller size, while the shape index distribution curves shift toward higher index. Therefore, the fragments become finer but more isotropic under the high strain rate loading compared to the quasi-static loading.

The means and standard deviations of the fragment size and shape parameters are derived for different strain rates, and the results are shown in **Fig. 5**. The mean fragment size remains approximately constant (~380 μm) under quasi-static loading, but decreases abruptly to ~160 μm under dynamic loading, consistent with previous studies [18, 32]. The constant fragment size under quasi-static loading is defined as the quasi-static size limit [32]. In addition, the standard deviations of the fragment size decrease from about 200 μm to 90 μm, when the strain rate increases from 0.001 s⁻¹ to 1000 s⁻¹. The standard deviations exhibit a logarithmic linear relationship with strain rate. Therefore, the range of fragment sizes becomes narrower under higher strain rates.

Based on the concepts of energy balance [30,31] or stress-wave interactions [32,68], several theoretical models have been proposed to predict the mean fragment size s under different strain rates $\dot{\epsilon}$. Here, two typical models, i.e. Glenn-Chudnovsky (G-C) model [31] and ZMR [32] empirical model, are selected to compare with the experimental data. The G-C and ZMR models link the normalized fragment size (\bar{s}) to the normalized strain rate ($\bar{\epsilon}$) as follows. The G-C normalized fragment size is,

$$\bar{s} = \frac{4}{\bar{\epsilon}} \sinh \left[\frac{1}{3} \sinh^{-1} \left(\frac{3}{2} \bar{\epsilon} \right) \right], \quad (7)$$

while the ZMR normalized fragment size is,

$$\bar{s} = \frac{4.5}{1 + 4.5 \bar{\epsilon}^{2/3}}, \quad (8)$$

where $\bar{s} = s/s_0$ and $\bar{\epsilon} = \dot{\epsilon}/\dot{\epsilon}_0$. $s_0 = EG_c/\sigma_t^2$ and $\dot{\epsilon}_0 = C\sigma_t^3/(E^2G_c)$ are characteristic fragment size and characteristic strain rate, respectively. Here, E is elastic modulus, G_c is fracture energy, σ_t is local tensile strength and C is longitudinal wave velocity. For alumina [18], $E = 410$ GPa, $G_c = 30$ N m⁻¹, $\sigma_t = 267$ MPa and $C = 10294$ m s⁻¹. s_0 and $\dot{\epsilon}_0$ are calculated as 172.5 μm and 38844 s⁻¹, respectively.

The G-C and ZMR models are also plotted in **Fig. 5a**, and exhibit similar evolution trend with the experimental data. However, they cannot describe quantitatively the experimental data in this work. The critical normalized strain rate is around 0.005 for the ZMR model, and is ~1 for the G-C model. The ZMR model predicts a comparable critical strain rate, but a considerably higher quasi-static size limit than the experimental data. In contrast, the G-C model predicts a consistent quasi-static size limit under quasi-static loading, but a far larger critical strain rate. Li et al. [69] have tried to modify the G-C model to match their experimental data on rocks. Although the modified model appears effective for rocks, it shows discrepancy with our data in both the quasi-static size limit and critical strain rate and thus not presented.

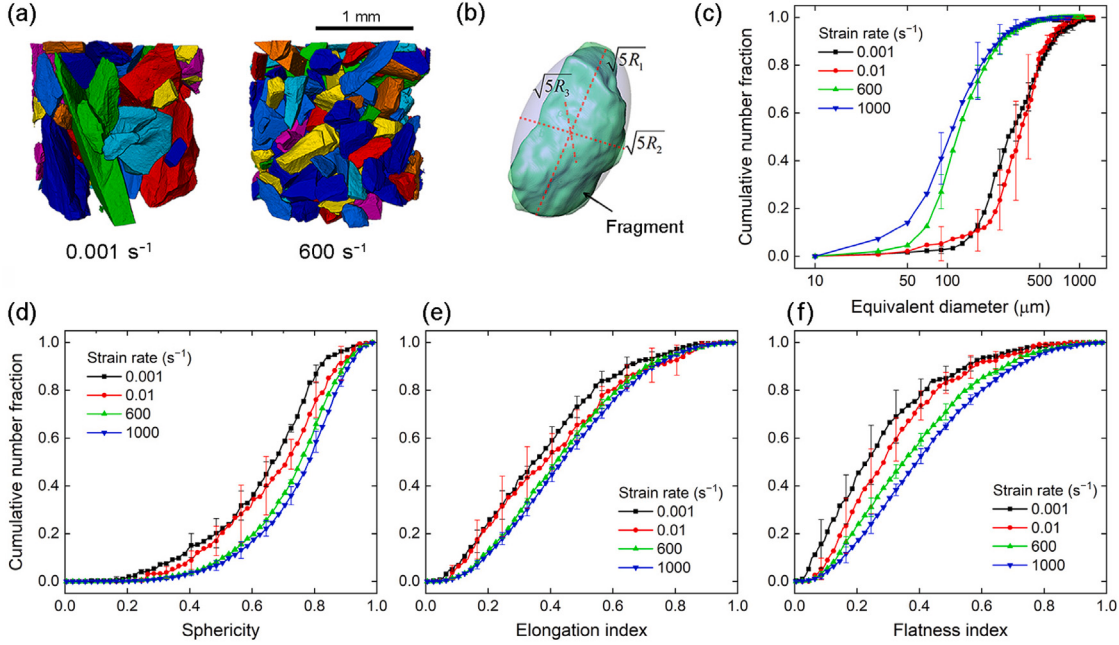


Fig. 4. CT characterizations and statistical morphology analysis of ceramic fragments at different strain rates. (a) Volume renderings of partial fragments at the 0.001 s^{-1} and 600 s^{-1} strain rates. (b) Schematic diagram of constructing a characteristic ellipsoid for a typical fragment via gyration tensor analysis. R_1 , R_2 and R_3 are eigenvalues of the gyration tensor of the fragment. (c)–(f) Equivalent diameter (c), sphericity (d), elongation index (e) and flatness index (f) distributions of fragments at four different strain rates as noted. Error bars refer to standard deviations for three repeat measurements.

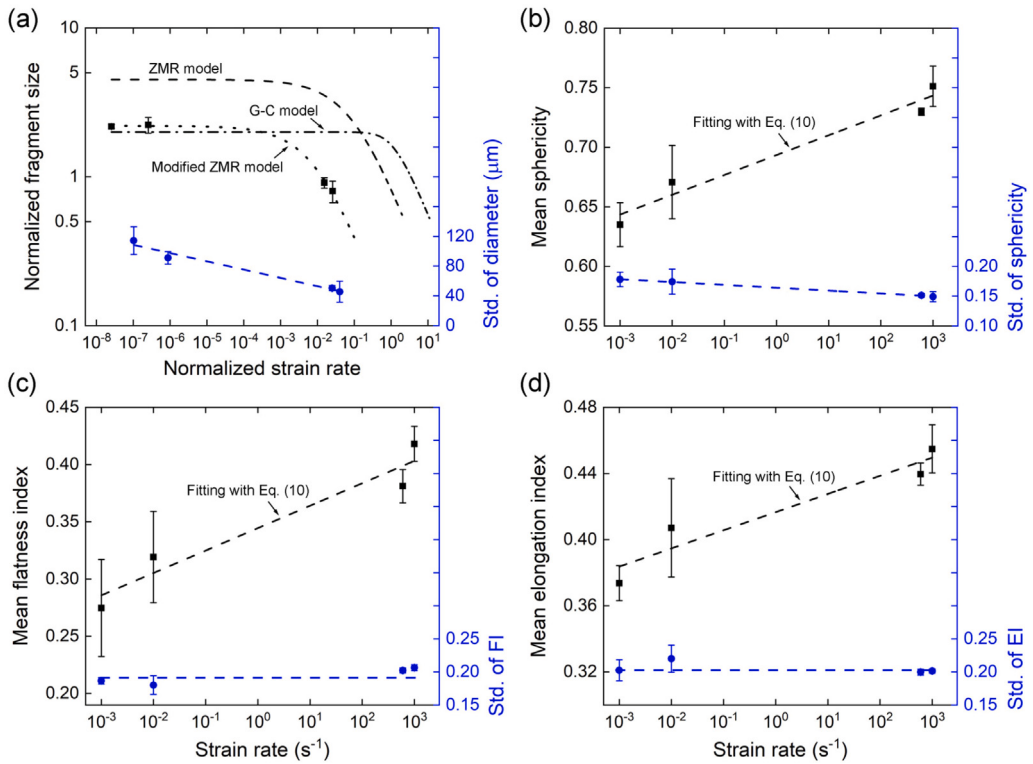


Fig. 5. Means and standard deviations (std.) of the fragment size and shape indices as a function of strain rate. (a) Equivalent diameter, (b) sphericity, (c) elongation index and (d) flatness index. In figure (a), the characteristic fragment size and strain rate are used for normalization. In figures (a)–(d), the points and error bars refer, respectively, to the means and standard deviations of the experimental data. The black curves are fitting to the experimental data, while the blue (dashed) curves are guides to the eye. The points and curves colored black belong to the left y axis, while those in blue, to the right y axis.

For simplicity, a modified ZMR model is proposed to describe the experimental data as,

$$\bar{s} = \frac{p_0}{1 + p_1 \bar{\epsilon}^{2/3}}, \quad (9)$$

where p_0 represents the quasi-static limit of the normalized fragment size, and is calculated as 2.21 using the quasi-static data. p_1 is a fitting parameter, and is fitted as 21.5 ± 1.4 . The experimental data agree well with the modified ZMR model. It is interesting to note the fracture

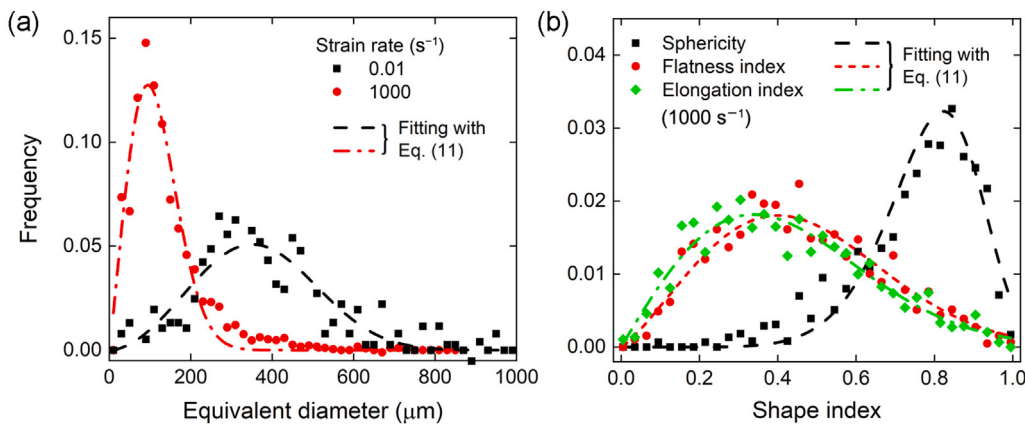


Fig. 6. Number frequency distributions of the fragment size and shape indices at representative strain rates as noted. (a) Equivalent diameter distributions at 0.001 s^{-1} and 1000 s^{-1} strain rates. (b) Sphericity, EI and FI distributions at 1000 s^{-1} strain rate. Points refer to experimental data, while curves, fitting results with the Weibull distribution.

Table 1

Weibull fitting parameters for the number frequency distributions of the equivalent diameter (size), sphericity, EI and FI of the fragments at different strain rates as noted. k : shape parameter; λ : scale parameter. Numbers in the brackets are fitting errors.

Strain rate (s^{-1})	Size parameters		Sphericity parameters		EI parameters		FI parameters	
	k	λ	k	λ	k	λ	k	λ
0.001	2.21 (0.16)	353.7 (15.1)	5.79 (0.41)	0.736 (0.009)	1.79 (0.11)	0.432 (0.021)	1.48 (0.09)	0.293 (0.019)
0.01	2.80 (0.20)	411.5 (12.2)	4.77 (0.44)	0.781 (0.016)	1.67 (0.14)	0.481 (0.037)	1.84 (0.11)	0.336 (0.016)
600	2.21 (0.13)	175.7 (6.1)	6.89 (0.81)	0.812 (0.003)	2.20 (0.06)	0.501 (0.008)	1.83 (0.05)	0.431 (0.009)
1000	2.11 (0.08)	128.4 (3.0)	7.65 (0.23)	0.837 (0.003)	2.22 (0.05)	0.525 (0.006)	1.99 (0.04)	0.480 (0.007)

strength and fragment size both exhibit a power-law scaling with the strain rate (Eqs. (3) and (9)), and the power is identically $2/3$. Therefore, the micromechanisms for the strain rate induced strengthening and fragment refinement are probably the same.

Apart from the fragment size, the shape indices of fragments also vary significantly with strain rate. The mean sphericity, EI and FI increase by 19%, 20% and 53%, respectively, when the strain rate increases from 0.001 s^{-1} to 1000 s^{-1} . Therefore, the fragments become more isotropic in 3D shapes under dynamic loading compared to quasi-static loading. In addition, they all exhibit a logarithmic linear relationship with strain rate. Then, a Johnson–Cook like model [70] is used to describe the strain rate effects on the mean sphericity, EI and FI of fragments, i.e.,

$$Y = Y_r \left[1 + c \ln \left(\frac{\dot{\epsilon}}{\dot{\epsilon}_r} \right) \right], \quad (10)$$

where Y denotes the physical variable under consideration, i.e., sphericity, EI or FI. Y_r is a reference value of Y at the reference strain rate $\dot{\epsilon}_r$. c is strain-rate sensitivity coefficient. Here, $\dot{\epsilon}_r$ is chosen as 0.001 s^{-1} . Then c and Y_r for sphericity, EI or FI can be obtained via nonlinear fitting with Eq. (10), as illustrated by the black dashed lines in Fig. 5b-d. The c -values for sphericity, EI and FI are 0.011 ± 0.002 , 0.012 ± 0.003 and 0.029 ± 0.007 , respectively, while the Y_r -values are 0.643 ± 0.010 , 0.384 ± 0.010 and 0.286 ± 0.016 , respectively. FI exhibits higher strain-rate sensitivity than sphericity and EI. In addition, the standard deviations of sphericity decrease slightly, while those of EI and FI remain approximately constant, with increasing strain rate.

The distribution curves reflect comprehensively the statistical features of fragments. It is meaningful to construct empirical models for the fragment size/shape distributions. Regarding the size distribution, the most frequently used function in the exponential-like form is the Weibull distribution [69,71]. The Weibull distribution has been demonstrated to describe well the fragment size distribution of both metals and brittle materials. So, it is naturally to examine whether the Weibull distribution can describe the fragment shape distribution. Then the size and shape distributions of fragment number frequency (f) are used to

examine the Weibull distribution in the form of probability distribution function (PDF),

$$f(X; \lambda, k) = f_0 \frac{k}{\lambda} \left(\frac{X}{\lambda} \right)^{k-1} \exp \left[- \left(\frac{X}{\lambda} \right)^k \right], \quad (11)$$

where X denotes to the physical variable under consideration, i.e., size, sphericity, EI or FI. k and λ are shape and scale parameters, respectively. f_0 is amplitude parameter. A larger k indicates a narrower distribution for $k > 1$ and constant λ .

The number frequency distributions of fragment size, sphericity, EI and FI at different strain rates are derived from the cumulative distributions (Fig. 4), and fitted with Eq. (11). The fitting results at some representative strain rates are presented in Fig. 6. It is noteworthy that the fragment size and shape distributions all conform well with the Weibull distribution. Therefore, the Weibull distribution is appropriate to describe the fragment morphology of ceramics across a wide range of strain rates. The fitted shape and scale parameters are summarized in Table 1. The amplitude parameter f_0 stays at 18.6 for fragment size and 0.009 for shape indices, regardless of strain rate, and hence is not listed for brevity. The shape parameter k varies considerably for different variables, and appears the largest for sphericity. With increasing strain rates (from 0.001 s^{-1} to 1000 s^{-1}), k remains approximately constant for the fragment size distribution, but increases by about 32%, 24% and 34% for the sphericity, EI and FI distributions, respectively. The scale parameters λ exhibit similar evolution trends to the corresponding means of fragment size and shape indices (Fig. 5), because the mean of the Weibull distribution is expressed as $\lambda \Gamma(1+1/k)$, where Γ is Gamma function. Therefore, the strain rate scaling laws for the means can also be applied to the scale parameter. With Eqs. (10) and (11), the fragment size or shape distributions at various strain rates can be predicted, and implemented in theoretical or numerical analysis.

To explore the size dependence of fragment shapes, the sphericity and elongation index of fragments are plotted against their equivalent diameter for different strain rates. Fig. 7a demonstrates that the sphericity-size data pairs of fragments are not uniformly distributed. With decreasing fragment size (in logarithmic coordinate), the scatter range of fragment sphericity becomes narrower and converges gradually to the upper left corner, as sketched by the shaded rectangle in

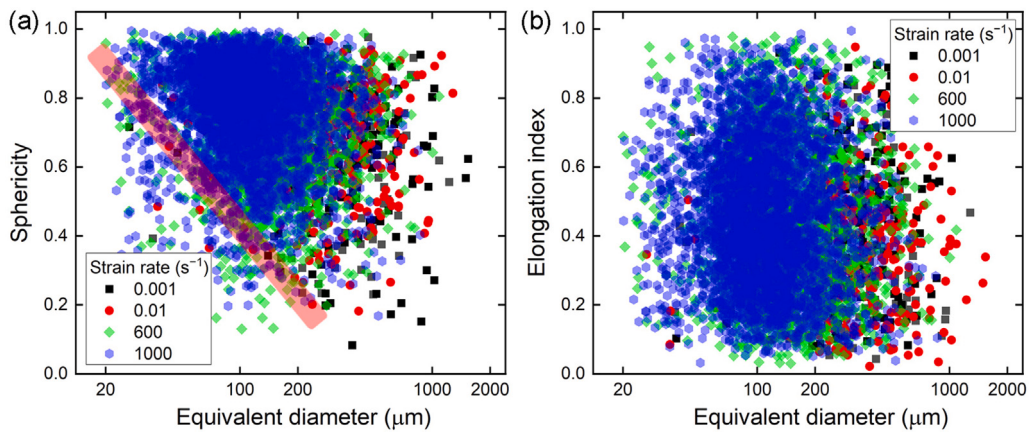


Fig. 7. Size dependence of the fragment shape indices at different strain rates as noted. (a) Sphericity, and (b) elongation index. Each point corresponds to a single fragment. The shaded rectangle in (a) is guide to the eye.

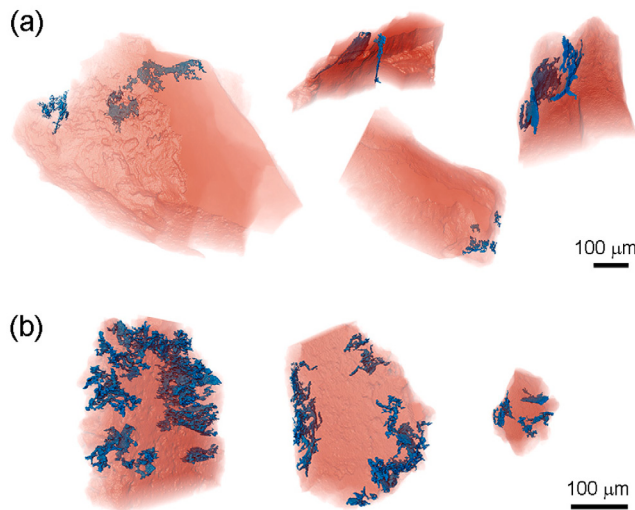


Fig. 8. Volume renderings of representative fragments with residual cracks under quasi-static and dynamic loading. (a) Quasi-static loading (0.001 s^{-1}). (b) Dynamic loading (1000 s^{-1}). In figure, the fragments are colored red with partial transparency, while the residual cracks are colored blue.

Fig. 7a. The number of data points is negligible below the shaded rectangle, indicating that fine fragments (mainly from dynamic fracture) tend to be statistically closer to spheres than coarse fragments. This is consistent with the previous 2D characterizations on silicon carbide fragments under dynamic compression in terms of the circularity-size relationship [72]. In contrast, the elongation index of fragments show little dependence on fragment size (as shown in Fig. 7b). In each size range, the elongation index of fragments spans approximately uniformly from 0 to 1.

Residual cracks are observed in part of the fragments, and are extracted from the 3D volume data. The volume renderings of some representative fragments with residual cracks are presented in Fig. 8 for quasi-static and dynamic loading. Under quasi-static loading (Fig. 8a), the residual cracks are mostly close to the fragment surface, and the density of such cracks is low. However, under dynamic loading (Fig. 8b), the density of residual cracks in the fragments appear considerably higher than that under quasi-static loading. This higher residual crack density is probably due to enhanced crack nucleation [66] but decelerated crack growth/propagation [54] during the rapid dynamic fragmentation process. A considerable number of micro cracks are frozen before coalescence due to the short loading pulse.

3.3. High-speed optical/X-ray imaging

To explore the underlying mechanisms of strain rate effects on fragment morphologies (Fig. 5), high-speed optical imaging [67] is conducted to capture the fragmentation process of the alumina under different strain rates. The stress histories along with optical images of the ceramic samples under quasi-static (0.001 s^{-1}) and dynamic (1000 s^{-1}) loading are presented in Fig. 9. Both stress histories are concave upward at low stress levels, but become approximately linear beyond about 1.0 GPa. The stress rate for quasi-static and dynamic loading is $\sim 1 \text{ GPa s}^{-1}$ (Fig. 9a) and $\sim 10^6 \text{ GPa s}^{-1}$ (Fig. 9b), respectively.

Under quasi-static loading, damage evolution occurs mainly around the peak stress, and six snapshots (frames 1–6, as marked in the inset of Fig. 9a) of the sample around the peak stress point are presented in Fig. 9c. The loading direction is from top to bottom. With increasing loading, damage occurs first in the upper left corner of the sample (marked by the dashed rectangle at frame 1), and accumulates there at frames 2 and 3. At frame 4, an axial splitting crack is observed to initiate at the bottom of the sample and propagates approximately along the loading direction (marked by the red arrow at frame 4). Meanwhile, the macroscopic stress begins to relax. As loading continues (frame 5), the splitting crack at frame 4 cuts through the sample with an increased opening displacement; new splitting cracks (marked by the red arrows at frame 5) appear beside the old one. In addition, oblique or wing cracks are generated adjacent to the splitting cracks (marked by the blue arrows at frame 5), mainly due to frictional shear deformation between splitting crack surfaces [21,35,73]. At frame 6, the existing cracks continue to open, and break the sample into multiple pieces (demarcated by the dashed curves), inducing an abrupt stress drop of the sample. The splitting cracks tend to produce coarse, elongated fragments, consistent with the CT characterizations (Fig. 4a).

As for dynamic loading (Fig. 9d), the sample remains intact at frames 1 and 2. At frame 3, damage occurs firstly at the two ends of the sample (marked by the two dashed rectangles) at about 3.0 GPa. As loading increases to the peak (frame 4), similar axial splitting cracks initiate at the impact end (close to the damaged site), and propagate into the sample approximately along the loading direction (marked by the red arrows at frame 4). Different from the quasi-static case, the splitting cracks are larger in number but shorter in length. Moreover, crack branching appears in these splitting cracks (marked by the blue arrows at frame 4) as a result of wing cracks, before the splitting cracks traverse the whole sample. Wing cracks bridge adjacent splitting cracks, and form a barrier to the propagation of splitting cracks. At frames 5 and 6, multiple splitting and wing cracks interact, shatter the sample and cause a catastrophic failure of the sample. However, the crack networks (as marked by the dashed rectangle at frame 5) become blurred and cannot be resolved due to a limited depth of focus [67].

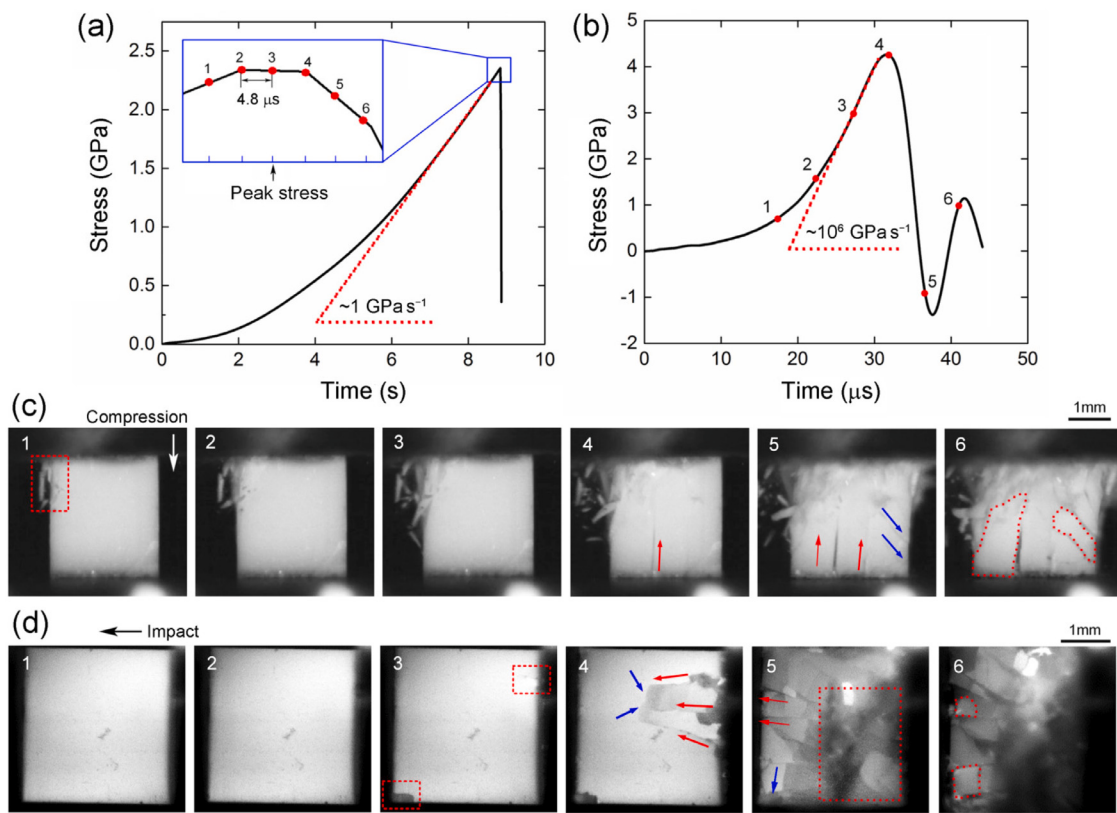


Fig. 9. *In situ*, high-speed optical imaging of the deformation and fracture processes of the alumina samples under quasi-static and dynamic loading. (a) and (b) Stress histories. The stress rate for quasi-static and dynamic loading is $\sim 1 \text{ GPa s}^{-1}$ and $\sim 10^6 \text{ GPa s}^{-1}$, respectively. (c) and (d) High-speed image sequences captured at selected instants (1–6) as noted in (a) inset and (b), respectively. The frame interval is about $4.8 \mu\text{s}$. (a) and (c) Quasi-static loading (0.001 s^{-1}). (b) and (d) Dynamic loading (1000 s^{-1}).

Compared to quasi-static loading, the crack density in the sample is considerably higher under dynamic loading, with more wing cracks and pronounced crack interactions.

To resolve clearly the crack networks, high-speed X-ray phase contrast imaging is adopted to capture the dynamic fracture process of ceramic samples. The X-ray phase contrast imaging is superior for resolving micro cracks due to edge enhancement and higher penetration capability [35,74]. The stress histories and X-ray images are presented in Fig. 10. The sample geometry and loading conditions are similar to those presented in Fig. 9d. As shown in Fig. 10b, the ceramic sample remains intact at frames 1 and 2. At frame 3, high-density cracks (white lines) are observed in the sample, with both horizontal splitting cracks (marked by the red arrows at frame 3) along the loading direction and wing cracks perpendicular to splitting cracks (marked by the blue arrows at frame 3). As loading proceeds, the splitting cracks continue to open, and more wing cracks (marked by the blue arrows at frame 4) are formed adjacent to those splitting cracks. These wing cracks promote the crack density under dynamic loading, leading to increased interactions between microcracks. The splitting cracks and wing cracks form a complex network to cut the sample into fine pieces.

3.4. SEM characterizations on fragments

In order to reveal the microscopic damage mechanisms, SEM characterizations are conducted on the ceramic fragments. Fig. 11 presents the SEM micrographs (in secondary electron mode) of fracture surfaces under quasi-static (0.001 s^{-1}) and dynamic (1000 s^{-1}) loading. Two typical micro or grain-scale damage modes of the alumina are observed: intergranular and transgranular fracture. These micro cracks act as a precursor to the macro cracks, and can tell how and where the splitting or wing cracks originate. The micro and macro cracks demonstrate the damage evolution at different scales and deformation stages.

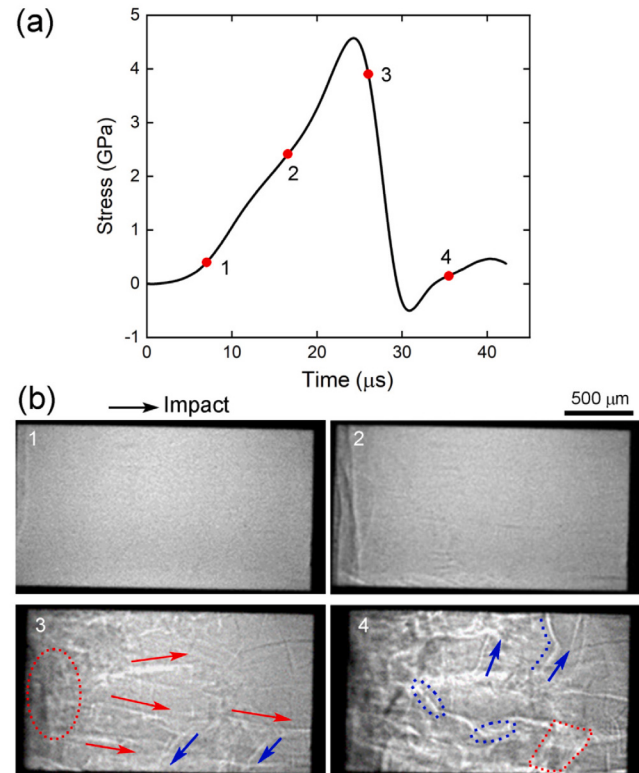


Fig. 10. *In situ*, high-speed X-ray imaging of the alumina samples under dynamic compression (1000 s^{-1}). (a) Stress history. (b) X-ray image sequences captured at selected instants (1–4) as noted in (a). The frame interval is $10 \mu\text{s}$.

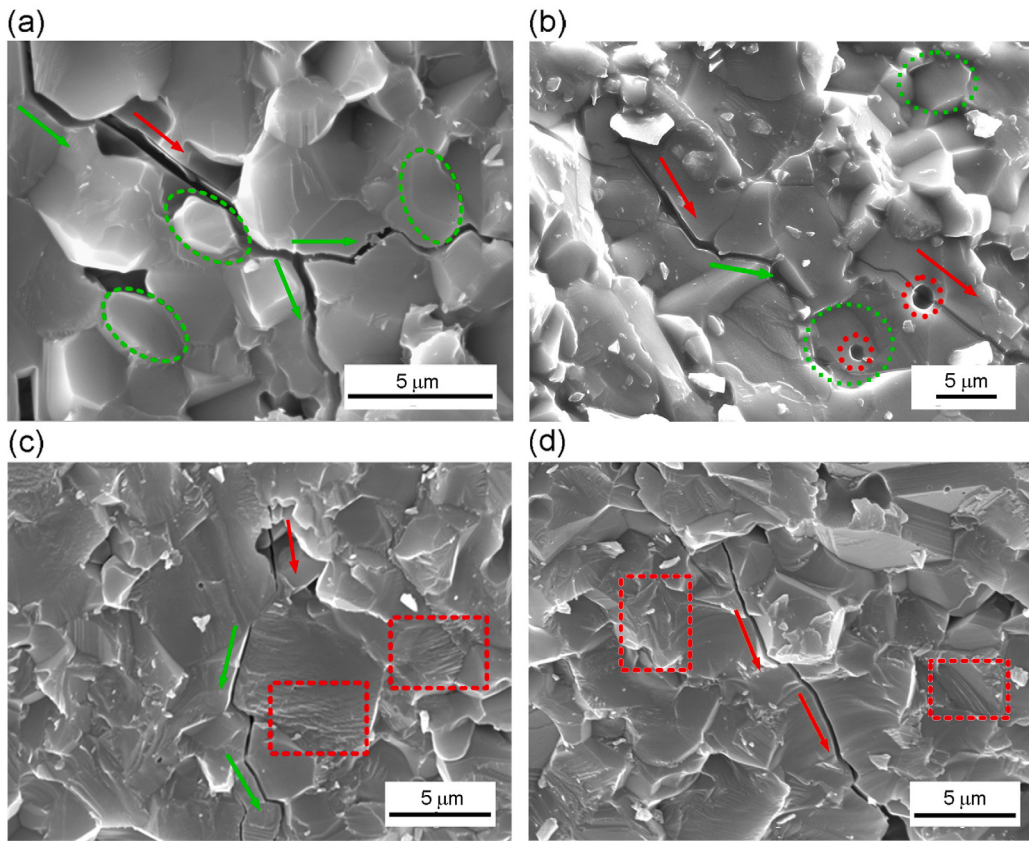


Fig. 11. SEM micrographs of the ceramic fragments at different strain rates. (a) and (b) Quasi-static loading (0.001 s^{-1}). (c) and (d) Dynamic loading (1000 s^{-1}).

Under quasi-static loading (Fig. 11a and b), a large number of undulations and smooth platforms (marked by the dashed green ellipses) can be seen across the fracture surfaces. Such smooth platforms are generally considered as a result of intergranular fracture [19,75]. In addition, residual cracks are also detected in the fracture surfaces, consistent with the CT characterizations (Fig. 8). Intergranular and transgranular cracks (marked by the green and red arrows, respectively) are both observed. The intergranular cracks appear tortuous with bifurcations, while transgranular cracks are relatively straight and barely change directions during propagation [76]. Therefore, the micro damage mode under quasi-static loading is mainly intergranular fracture. The few transgranular cracks act mainly as a bridge for coalescence of intergranular cracks. Apart from grain boundaries, initial pores are found to play an important role in the micro damage of ceramics [33,76], as illustrated in Fig. 11b. Specifically, two pores marked by the red dashed circles participate in micro damage evolution. One of them is penetrated by a transgranular crack, while the other is located on an intergranular crack plane. Therefore, initial pores induce both intergranular and transgranular fracture. For dynamic loading (Fig. 11c and d), the fracture surfaces are relatively flat with few undulations and platforms. Instead, many stripes or river-like patterns are seen across the fracture surfaces (marked by the dashed boxes), which are signals of cleavage fracture [19,65,77]. Therefore, transgranular fracture dominates the micro damage of ceramic samples under dynamic loading [65,78].

3.5. Further discussions

The size and shape of the recovered fragments change with strain rate, and such changes are mainly attributed to the change in microscopic fracture modes of the alumina under different strain rates. Optical/X-ray imaging (Figs. 9 and 10) and SEM analysis (Fig. 11) reveal obvious difference in damage and fracture modes under dynamic

and quasi-static loading, as sketched in Fig. 12. Red ellipses refer to micro cracks, while black strips, primary/secondary wing cracks (PWCs/SWCs).

Under quasi-static loading (Fig. 12a), micro cracks prefer to initiate at the weak zones of sample (flaws, pores, grain boundaries, etc.) [37, 66]. Such micro cracks are oriented at nearly 45° with respect to the loading direction, due to compression induced shear. PWCs, oriented approximately along the loading direction, tend to form at the tips of these micro cracks, as described by the sliding crack model [79]. These wing cracks grow, interact and coalesce, inducing the axial splitting cracks (marked by the solid arrows) observed in the experiment (Fig. 5a). The splitting cracks penetrate the sample and spit it into coarse, strip-shaped fragments. Hence, the mean sphericity, EI and FI of the fragments are low as well (Fig. 5). In addition, the oblique cracks under quasi-static loading (Fig. 9a) may be attributed to either secondary wing cracking at the PWC tips (marked by the empty arrows) [35] or shear-driven growth and propagation of the micro cracks (marked by the dashed circles). Nevertheless, the number of secondary wing cracks is low, probably due to rapid lateral expansion and little relative movement between crack surfaces [80]. However, under dynamic loading (beyond the critical strain rate, Fig. 12b), the number of micro cracks rises significantly as a result of more random nucleation of damage across the sample [66,81], resulting in a greater number of PWCs. In addition, a large number of secondary wing cracks initiate at the tips of PWCs owing to violent local movement, inducing pronounced crack branching and bridging (marked by the dashed ellipses and arrows, respectively). Crack branching and bridging promotes the global crack density of sample, and suppresses the coalescence of PWCs into axial splitting cracks. The high-density PWCs and SWCs form a crack network dividing the sample into fine pieces. As a result, more cuboidal (quasi-spherical) fragments are produced (as marked by the empty arrows), leading to higher mean sphericity, EI and FI of the fragments. Therefore, the fine fragments produced by coalescence of

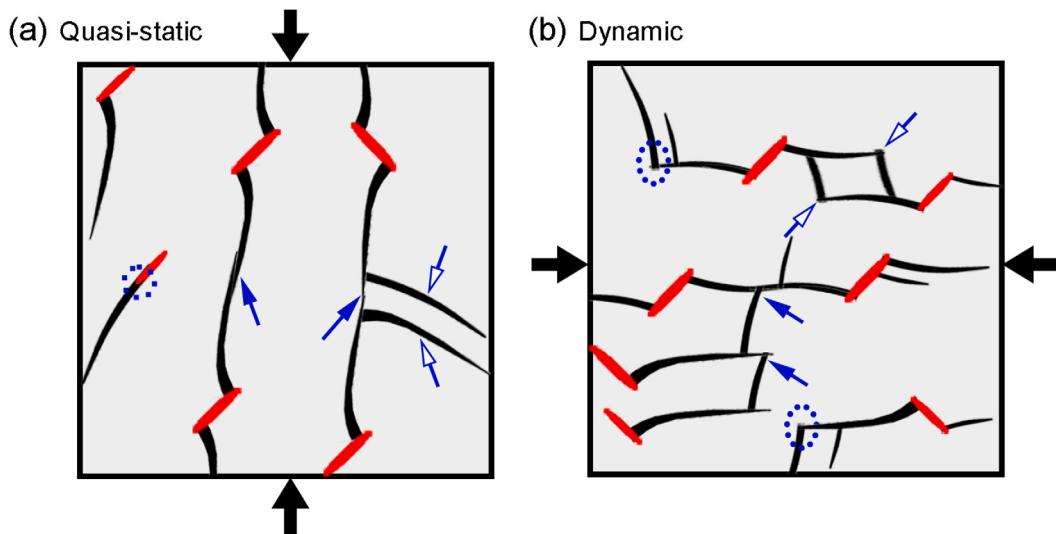


Fig. 12. Schematic diagrams for damage and fracture modes of ceramic samples (light gray areas) at different strain rates. (a) Quasi-static loading, and (b) dynamic loading. In figure, red ellipses refer to micro cracks, while black strips, primary/secondary wing cracks. For comparison, loading directions (marked by the arrows at the border) are set consistent with those in the corresponding experiments.

multiple splitting and wing cracks appear more spherical or isotropic, irrespective of quasi-static or dynamic loading. This explains the size dependence of fragment sphericity shown in Fig. 7a.

The strain-rate dependence on the micro damage modes (Fig. 11) can be elucidated qualitatively according to the classic nucleation theory [81]. Since the loading rate is low under quasi-static loading, deformation and damage are prone to concentrate at the weak zones, and have sufficient time to grow along grain boundaries in the form of intergranular fracture [82]. However, under dynamic loading, the nucleation sites of damage become more randomly distributed to accommodate rapidly the external deformation due to the high loading rate and driving force, as manifested by the X-ray digital image correlation [58,59] and CT-based numerical simulations [37,52,66]. In addition, micro damage or cracks have no time to propagate along the path with the lowest “cohesive” strength [68,83], but propagate in a way that is more conducive to stress or energy release [84]. That is, micro cracks propagate mainly along the local maximum shear or tension direction (irrespective of grain boundaries), in a mixed mode of transgranular and intergranular fracture. Transgranular fracture hence dominates the micro damage of sample under dynamic loading. Furthermore, the change in micro damage modes also promotes the fracture strength of the alumina under high strain rate loading (Fig. 3). Transgranular fracture requires a higher driving force at the micro scale, and contributes to a higher fracture resistance at the macro scale. Apart from the damage mode transition, inertial effects related to dynamic crack propagation also promote the dynamic fracture strength [31]. The inertial effects slow down the damage evolution (in terms of strain) and enhance the crack density and crack interactions. The increased crack density produces more surface areas, leading to higher energy consumption (in the form of surface energy and frictional dissipation) during the fracture process of ceramic samples [31], resulting in a higher macroscopic stress at failure. However, inertial effects associated with lateral confinement which were widely reported in concrete [66,85], have little influence on the fracture strength of ceramics, as argued in Ref. [17]. The transgranular fracture and crack-propagation related inertial effects mutually contribute to the increased strain rate sensitivity of the alumina under high strain rate loading (Fig. 3).

Extensive efforts [17,54,86,87] have been devoted to developing micromechanics models for brittle materials, based on the sliding crack model [79]. Such models can bridge cracking features with fracture strength. The cracking features, such as length and density of critical

cracks (leading to sample failure), are generally difficult to measure directly from experiments, but may be deduced from the fragment morphologies presented in this work. On one hand, numerical modeling suggested that the length of critical cracks became much smaller under high strain rate loading [54], as manifested by the smaller dynamic fragment size. Thus, the evolution of the critical crack length with strain rate can be derived from the strain rate dependence of fragment size (Fig. 5), and is then correlated to fracture strength. In fact, the rate dependence of fragment size and fracture strength shares similar power-law forms with the same power of 2/3 (Eqs. (3) and (9)). On the other hand, the fragment shape appears more isotropic at higher strain rates, owing to an increased density of wing cracks and enhanced crack interactions under dynamic loading. Likewise, the evolution of the critical crack density with strain rate can be associated with the strain rate dependence of fragment shape indices, and implemented in the micromechanics model of fracture strength.

4. Conclusions

In summary, the fracture strength, 3D fragment morphologies and fracture mechanisms of the alumina ceramic under quasi-static to dynamic loading ($0.001\text{--}1000\text{ s}^{-1}$) are investigated using a variety of techniques including SHPB, synchrotron micro CT and high-speed optical/X-ray imaging. The fracture strength increases in a power-law form with the strain rate. The fragment size and shape distributions follow the same Weibull probability distribution function, with the fitted shape and scale parameters varying considerably with strain rate and fragment morphology. The mean fragment size remains approximately constant at $\sim 380\text{ }\mu\text{m}$ under quasi-static loading, but decreases abruptly to around $160\text{ }\mu\text{m}$ under dynamic loading, which can be well described by the modified ZMR model. The fragment size and fracture strength both exhibit a power-law scaling with strain rate, and the powers are identically 2/3. In addition, the scatter of the fragment sizes descends gradually with ascending strain rates.

The mean sphericity, EI and FI of the fragments increase by about 19%, 20% and 53%, respectively, when the strain rate increases from 0.001 s^{-1} to 1000 s^{-1} . Moreover, these three shape indices all exhibit a logarithmic linear relationship with the strain rate. Therefore, the fragments generated by high strain rate loading appear finer and more isotropic compared to those by quasi-static loading. In addition, with descending fragment sizes, the sphericity of the fragments (with a specific size) increases on average, indicating that fine fragments

tend to be statistically closer to spheres than coarse fragments. In contrast, the elongation/flatness index of fragments shows negligible dependence on the fragment size. Residual cracks are detected in some of the fragments. The density of residual cracks in the fragments under dynamic loading is considerably higher than that under quasi-static loading, due to a more severe but rapid fragmentation process under dynamic loading.

The underlying mechanisms for the strain rate effects on the fragment morphologies of the alumina are revealed by high-speed optical/X-ray imaging along with SEM. Primary and secondary wing cracks are seen to control the fracture and fragmentation process of ceramic samples. Under quasi-static loading, coalescence of PWCs induces axial splitting cracks which penetrate the sample and produce coarse, elongated fragments. In contrast, the density of PWCs and SWCs becomes considerably higher across the sample under dynamic loading, resulting in stronger crack interactions. The PWCs and SWCs form a complex network to cut the sample into fine pieces, which contribute to the higher sphericity, EI and FI of the fragments. At the micro scale, intergranular fracture dominates the micro damage of ceramic samples under quasi-static loading, while transgranular fracture, under dynamic loading, as a result of more homogeneous nucleation and growth of micro damage induced by a high driving force and deformation rate. The transgranular fracture along with crack-propagation related inertial effects mutually contribute to the increased strain rate sensitivity of the alumina under high strain rate loading.

CRediT authorship contribution statement

J.Y. Huang: Writing – review & editing, Writing – original draft, Project administration, Funding acquisition, Formal analysis, Data curation, Conceptualization. **C.K. Lin:** Visualization, Methodology, Data curation. **Y.L. Bian:** Investigation. **H.L. Xie:** Resources, Methodology. **H.W. Chai:** Validation, Software, Methodology, Investigation. **Y.Y. Ding:** Writing – review & editing, Investigation. **S.N. Luo:** Writing – review & editing, Supervision, Resources, Funding acquisition.

Declaration of competing interest

The authors declare that they have no known competing financial interests or personal relationships that could have appeared to influence the work reported in this paper.

Data availability

Data will be made available on request.

Acknowledgments

We would like to thank the Editor and anonymous reviewers for providing constructive comments on this manuscript. This work was partially supported by National Natural Science Foundation of China (Grant Nos. 12172312 and 11627901), Zhejiang Provincial Natural Science Foundation of China (Grant No. LY24A020001).

Appendix

In this work, a series of facilities/techniques are utilized to characterize the mechanical properties and microstructures (before and after loading) of the alumina ceramic. For clarity, a flowchart of the technical routes and corresponding facilities/techniques used is presented in Fig. A.1. The core content of the work (marked red) is statistical analysis of the 3D fragment morphologies via synchrotron CT, and to elucidate the strain rate effects (model and mechanisms) on fragment morphology using the *in situ* optical/X-ray imaging and SEM.

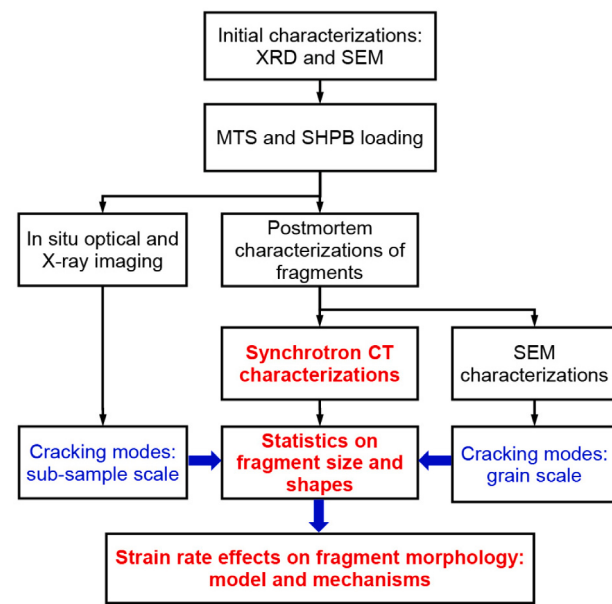


Fig. A.1. Flowchart of the technical routes and corresponding experimental techniques used in this work. The core contents of this work are marked red.

References

- [1] Farbaniec L, Hogan JD, Ramesh KT. Micromechanisms associated with the dynamic compressive failure of hot-pressed boron carbide. *Scr Mater* 2015;106:52–6.
- [2] Huang JY, Yuan JC, Zhu TT, Zhong T, Xu YF, Luo SN. Dynamic compressive strength of alumina ceramics. *Ceram Int* 2022;48(24):36371–82.
- [3] Zheng J, Ji M, Zaiemeykeh Z, Li H, Hogan JD. Strain-rate-dependent compressive and compression-shear response of an alumina ceramic. *J Eur Ceram Soc* 2022;42(16):7516–27.
- [4] Boldin MS, Berendeev NN, Melekhin NV, Popov AA, Nokhrin AV, Chuvildeev VN. Review of ballistic performance of alumina: Comparison of alumina with silicon carbide and boron carbide. *Ceram Int* 2021;47(18):25201–13.
- [5] Tian C, Sun Q, An X, Ye P, Dong Y. Influences of ceramic constraint on protection performances of ceramic-metal hybrid structures under impact loads. *Int J Mech Sci* 2019;159:81–90.
- [6] Andraskar ND, Tiwari G, Goel MD. Impact response of ceramic structures-A review. *Ceram Int* 2022;48:27262–79.
- [7] Li J, Qin Q, Zhang J. Internal blast resistance of sandwich cylinder with lattice cores. *Int J Mech Sci* 2021;191:106107.
- [8] Zhang J, Qin Q, Wang Z, Ai W, Wang T. A theoretical study of plastic analysis of fully clamped geometrical asymmetric sandwich beams with a metal foam core. *Int J Mech Sci* 2015;99:98–111.
- [9] Meng F, Yu T, Wiercigroch M, Wang Z, Cui Z, Liang Y, Wang Z, Zhao J. Profile prediction for ultrasonic vibration polishing of alumina ceramics. *Int J Mech Sci* 2023;252:108360.
- [10] Dresch AB, Venturini J, Arcaro S, Montedo ORK, Bergmann CP. Ballistic ceramics and analysis of their mechanical properties for armour applications: A review. *Ceram Int* 2021;47(7):8743–61.
- [11] Zou G, Wu S, Yan A, Chang Z, Li Y, Zhang Z. Penetration resistance of ceramic/PUE/GFRP multi-layered composite structure. *Compos Struct* 2023;311:116822.
- [12] Tian C, Li Z, Dong Y. Ballistic performance of hybrid structure with perforated panel. *Int J Mech Sci* 2022;218:107031.
- [13] Medvedovski E. Ballistic performance of armour ceramics: Influence of design and structure. Part 1. *Ceram Int* 2010;36(7):2103–15.
- [14] Xu Q, Feng J, Zhang S. Effects of different loads on structure stress of “L”-type large-diameter buried pipe network based on fluid-structure-heat coupling. *Int Commun Heat Mass Transfer* 2017;86:222–30.
- [15] Xu Q, Feng J, Liu L, Zhou J, Ye G, Chang C. Analysis of mechanical-fluid-thermal performance of heat pipeline system with structural deformation effects. *Int J Heat Mass Transfer* 2019;128:12–23.
- [16] Cheng M, Chen W. Measurement and determination of dynamic biaxial flexural strength of thin ceramic substrates under high stress-rate loading. *Int J Mech Sci* 2005;47(8):1212–23.
- [17] Kimberley J, Ramesh KT, Daphalapurkar NP. A scaling law for the dynamic strength of brittle solids. *Acta Mater* 2013;61(9):3509–21.

- [18] Zhang Q, Zheng Y, Zhou F, Yu T. Fragmentations of alumina (Al_2O_3) and silicon carbide (SiC) under quasi-static compression. *Int J Mech Sci* 2020;167:105119.
- [19] Ji M, Li H, Zheng J, Yang S, Zaiemykeh Z, Hogan JD. An experimental study on the strain-rate-dependent compressive and tensile response of an alumina ceramic. *Ceram Int* 2022;48(19):28121–34.
- [20] Zheng J, Li H, Hogan JD. Strain-rate-dependent tensile response of an alumina ceramic: Experiments and modeling. *Int J Impact Eng* 2023;173:104487.
- [21] Miao C, Xu S, Yuan L, Chen M, Xie Y, Wang P. Experimental investigation of failure diffusion in brittle materials subjected to low-speed impact. *Int J Mech Sci* 2023;259:108632.
- [22] Ning J, Ren H, Guo T, Li P. Dynamic response of alumina ceramics impacted by long tungsten projectile. *Int J Impact Eng* 2013;62:60–74.
- [23] Kudryavtsev OA, Sapozhnikov SB. Numerical simulations of ceramic target subjected to ballistic impact using combined DEM/FEM approach. *Int J Mech Sci* 2016;114:60–70.
- [24] Hogan JD, Farbaniec L, Mallick D, Domnich V, Kuwelkar K, Sano T, McCauley JW, Ramesh KT. Fragmentation of an advanced ceramic under ballistic impact: Mechanisms and microstructure. *Int J Impact Eng* 2017;102:47–54.
- [25] Holmquist TJ, Johnson GR. A computational constitutive model for glass subjected to large strains, high strain rates and high pressures. *J Appl Mech* 2011;78(5):051003.
- [26] Huang JY, Lu L, Fan D, Sun T, Fezzaa K, Xu SL, Zhu MH, Luo SN. Heterogeneity in deformation of granular ceramics under dynamic loading. *Scr Mater* 2016;111:114–8.
- [27] Crum RS, Homel MA, Pagan DC, Herbold EB, Miller D, Lind J, Jensen BJ, Iverson AJ, Akin MC. In situ X-ray imaging of heterogeneity in dynamic compaction of granular media. *J Appl Phys* 2019;125(2):025902.
- [28] Ramasamy A, Hill AM, Masouros S, Gibb I, Bull AMJ, Clasper JC. Blast-related fracture patterns: a forensic biomechanical approach. *J R Soc Interface* 2011;8(58):689–98.
- [29] Mathews ZR, Koyfman A. Blast injuries. *J Emerg Med* 2015;49(4):573–87.
- [30] Grady DE. Local inertial effects in dynamic fragmentation. *J Appl Phys* 1982;53(1):322–5.
- [31] Glenn LA, Chudnovsky A. Strain-energy effects on dynamic fragmentation. *J Appl Phys* 1986;59(4):1379–80.
- [32] Zhou FH, Molinari J-F, Ramesh KT. A cohesive model based fragmentation analysis: effects of strain rate and initial defects distribution. *Int J Solids Struct* 2005;42(18–19):5181–207.
- [33] Levy S, Molinari JF. Dynamic fragmentation of ceramics, signature of defects and scaling of fragment sizes. *J Mech Phys Solids* 2010;58(1):12–26.
- [34] Hogan JD, Farbaniec L, Shaeffer M, Ramesh KT. The effects of microstructure and confinement on the compressive fragmentation of an advanced ceramic. *J Am Ceram Soc* 2015;98(3):902–12.
- [35] Huang JY, Huang JW, Sun T, Fezzaa K, Xu SL, Luo SN. Dynamic deformation and fracture of single crystal silicon: Fracture modes, damage laws, and anisotropy. *Acta Mater* 2016;114:136–45.
- [36] Jiang S, Shen L, Guillard F, Einav I. Fracture and fragmentation patterns within a single cemented glass bead under impact. *Int J Impact Eng* 2019;131:152–61.
- [37] Huang Y, Yang Z, Ren W, Liu G, Zhang C. 3D meso-scale fracture modelling and validation of concrete based on in-situ X-ray computed tomography images using damage plasticity model. *Int J Solids Struct* 2015;67:340–52.
- [38] Huang Y, Guo F, Zhang H, Yang Z. An efficient computational framework for generating realistic 3D mesoscale concrete models using micro X-ray computed tomography images and dynamic physics engine. *Cem Concr Compos* 2022;126:104347.
- [39] Guo F, Zhang H, Yang Z, Huang Y, Withers PJ. A spherical harmonic-random field coupled method for efficient reconstruction of CT-image based 3D aggregates with controllable multiscale morphology. *Comput Method Appl Mech Eng* 2023;406:115901.
- [40] Zhou X, Dai N, Cheng X, Thompson A, Leach R. Three-dimensional characterization of powder particles using X-ray computed tomography. *Addit Manuf* 2021;40:101913.
- [41] Zanini F, Carmignato S. X-ray computed tomography for advanced geometrical measurements of metal powders and enhanced surface topography analyses of additively manufactured parts. *Powder Technol* 2022;412:118011.
- [42] Zhou B, Wang J, Zhao B. Micromorphology characterization and reconstruction of sand particles using micro X-ray tomography and spherical harmonics. *Eng Geol* 2015;184:126–37.
- [43] Li HY, Chai HW, Xiao XH, Huang JY, Luo SN. Fractal breakage of porous carbonate sand particles: microstructures and mechanisms. *Powder Technol* 2020;363:112–21.
- [44] Orosz Á, Angelidakis V, Bagi K. Surface orientation tensor to predict preferred contact orientation and characterise the form of individual particles. *Powder Technol* 2021;394:312–25.
- [45] Chai HW, Fan D, Yuan JC, Hu L, Xie HL, Du GH, Feng QJ, Zhou W, Huang JY. Deformation dynamics of a neutron-irradiated aluminum alloy: An in situ synchrotron tomography study. *Acta Mater* 2023;243:118493.
- [46] Yao Y, Chai HW, Li C, Bie BX, Xiao XH, Huang JY, Qi ML, Luo SN. Deformation and damage of sintered low-porosity aluminum under planar impact: microstructures and mechanisms. *J Mater Sci* 2018;53(6):4582–97.
- [47] Chai HW, Xie ZL, Xiao XH, Xie HL, Huang JY, Luo SN. Microstructural characterization and constitutive modelling of deformation of closed-cell foams based on in situ x-ray tomography. *Int J Plast* 2020;131:102730.
- [48] Chai HW, Xie ZL, Feng ZD, Luo SN, Huang JY. Three-dimensional deformation dynamics of porous titanium under uniaxial compression. *Mater Charact* 2021;182:111494.
- [49] Cheng JC, Chai HW, Fan GL, Li ZQ, Xie HL, Tan ZQ, Bie BX, Huang JY, Luo SN. Anisotropic spall behavior of CNT/2024Al composites under plate impact. *Carbon* 2020;170:589–99.
- [50] Bian YL, Chai HW, Ye SJ, Xie HL, Yao XH, Cai Y. Compression and spallation properties of polyethylene terephthalate under plate impact loading. *Int J Mech Sci* 2021;211:106736.
- [51] Bie BX, Pan RC, Xu J, Chai HW, Chen S, Du GH, Bian YL, Cai Y, Luo SN. Dynamic compression and fracture of poly (ether-ether-ketone) under plate impact. *Int J Mech Sci* 2023;246:108138.
- [52] Huang Y, Natarajan S, Zhang H, Guo F, Xu S, Zeng C, Zheng Z. A CT image-driven computational framework for investigating complex 3D fracture in mesoscale concrete. *Cem Concr Compos* 2023;143:105270.
- [53] Bontaz-Carion J, Pellegrini Y-P. X-ray microtomography analysis of dynamic damage in tantalum. *Adv Energy Mater* 2006;8(6):480–6.
- [54] Paliwal B, Ramesh KT. An interacting micro-crack damage model for failure of brittle materials under compression. *J Mech Phys Solids* 2008;56(3):896–923.
- [55] Chen R, Liu P, Xiao T, Xu LX, et al. X-ray imaging for non-destructive microstructure analysis at SSRF. *Adv Mater* 2014;26(46):7688–91.
- [56] Ono S, Brodholt JP, Price GD. First-principles simulation of high-pressure polymorphs in MgAl2O4. *Phys Chem Miner* 2008;35(7):381–6.
- [57] Lopatnikov SL, Gama BA, Krauthouser K, Gillespie G. Applicability of the classical analysis of experiments with split Hopkins pressure bar. *Tech Phys Lett* 2004;30(2):102–5.
- [58] Zhao JH, Xie ZL, Zhong T, Sun T, Fezzaa K, Cai Y, Huang JY, Luo SN. Strain rate effects on the mechanical behavior of porous titanium with different pore sizes. *Mater Sci Eng A* 2021;821:141593.
- [59] Ye SJ, Bie BX, Zhang ZM, Zhao XJ, Sun T, Fezzaa K, Huang JY, Yao XH, Luo SN. Rate-dependent strength and deformation heterogeneity of B4C-reinforced Al composite: Time-resolved imaging with synchrotron X-rays. *Ceram Int* 2021;53(3):105–28.
- [60] Li Y, Huang J, Fan D, Lu L, Zhang B, Zhong T, Dai B, Zhang S, Tao Y, Zhang Y, Chen S, Luo SN. Deformation twinning in single-crystal Mg under high strain rate tensile loading: A time-resolved X-ray diffraction study. *Int J Mech Sci* 2022;220:107106.
- [61] Chen RC, Dreossi D, Mancini L, Menk R, Rigon L, Xiao TQ, Longo R. PITRE: Software for phase-sensitive X-ray image processing and tomography reconstruction. *J Synchrotron Radiat* 2012;19(5):836–45.
- [62] Mizutani R, Saiga R, Takekoshi S, Inomoto C, Nakamura N, Itokawa M, Arai M, Oshima K, Takeuchi A, Uesugi K, Terada Y, Suzuki Y. A method for estimating spatial resolution of real image in the Fourier domain. *J Microsc* 2016;261(1):57–66.
- [63] Vincent L, Soille P. Watersheds in digital spaces: an efficient algorithm based on immersion simulations. *IEEE Trans Pattern Anal* 1991;(6):583–98.
- [64] Meyer F, Beucher S. Morphological segmentation. *J Vis Commun Image Represent* 1990;1(1):21–46.
- [65] Wang Z, Li R, Song W. Dynamic failure and inelastic deformation behavior of SiC ceramic under uniaxial compression. *Ceram Int* 2020;46(1):612–7.
- [66] Huang Y, Yang Z, Chen X, Liu G. Monte Carlo simulations of meso-scale dynamic compressive behavior of concrete based on X-ray computed tomography images. *Int J Impact Eng* 2016;97:102–15.
- [67] Miao C, Xu S, Lu J, Yuan L, Wang P. Dynamic breakage of double glass spheres chain subjected to impacting loading. *Int J Mech Sci* 2022;232:107610.
- [68] Zhou F, Molinari J-F, Ramesh K. Effects of material properties on the fragmentation of brittle materials. *Int J Fract* 2006;139(2):169–96.
- [69] Li X, Li H, Zhang Q, Jiang J, Zhao J. Dynamic fragmentation of rock material: characteristic size, fragment distribution and pulverization law. *Eng Fract Mech* 2018;199:739–59.
- [70] Johnson GR, Cook WH. A constitutive model and data for metals subjected to large strains, high strain rates and high temperatures. In: Proceedings of the 7th international symposium on ballistics. Vol. 21, The Netherlands: The Hague; 1983, p. 541–7.
- [71] Rosin P, Rammeler E. The laws governing the fineness of powdered coal. *J Inst Fuel* 1933;7(31):29–36.
- [72] Hogan JD, Farbaniec L, Daphalapurkar N, Ramesh KT. On compressive brittle fragmentation. *J Am Ceram Soc* 2016;99(6):2159–69.
- [73] Shen Q, Yang G, Xiao C, Song Q, Li H, Yao X, Fu M. A microcracking-based model for the dynamic failure of carbon/carbon composites. *Int J Mech Sci* 2023;260:108625.
- [74] Feng ZD, Zhou YH, Tan R, Hou HM, Sun T, Fezzaa K, Huang JY, Luo SN. Dynamic damage and fracture of a conductive glass under high-rate compression: A synchrotron based study. *J Non-Cryst Solids* 2018;494:40–9.
- [75] Liu X, Zou B, Xing H, Huang C. The preparation of $\text{ZrO}_2\text{-Al}_2\text{O}_3$ composite ceramic by SLA-3D printing and sintering processing. *Ceram Int* 2020;46(1):937–44.

- [76] Acharya S, Bysakh S, Parameswaran V, Mukhopadhyay AK. Deformation and failure of alumina under high strain rate compressive loading. *Ceram Int* 2015;41(5):6793–801.
- [77] Jiang W, Cheng X, Xiong Z, Ma Z, Ali T, Cai H, Zhang J. Static and dynamic mechanical properties of Yttrium Aluminum Garnet (YAG). *Ceram Int* 2019;45(9):12256–63.
- [78] Wang Z, Li P, Song W. Inelastic deformation micromechanism and modified fragmentation model for silicon carbide under dynamic compression. *Mater Des* 2018;157:244–50.
- [79] Brace WF, Bombolakis EG. A note on brittle crack growth in compression. *J Geophys Res* 1963;68(12):3709–13.
- [80] Dang-Trung H, Keilegavlen E, Berre I. Numerical modeling of wing crack propagation accounting for fracture contact mechanics. *Int J Solids Struct* 2020;204:233–47.
- [81] Cai Y, Huang JY, Wu HA, Zhu MH, Goddard III WA, Luo SN. Tensile strength of liquids: equivalence of temporal and spatial scales in cavitation. *J Phys Chem Lett* 2016;7(5):806–10.
- [82] Zavattieri PD, Espinosa HD. Grain level analysis of crack initiation and propagation in brittle materials. *Acta Mater* 2001;49(20):4291–311.
- [83] Zhang H, Huang YJ, Xu SL, Hu XJ, Zheng ZS. 3D cohesive fracture of heterogeneous CA-UHPC: A mesoscale investigation. *Int J Mech Sci* 2023;249:108270.
- [84] Zheng Y, Zhou F, Yu T. The fastest unloading in dynamic fragmentation events. *Sci Sin Technol* 2016;46(4):332.
- [85] Li QM, Meng H. About the dynamic strength enhancement of concrete-like materials in a split Hopkinson pressure bar test. *Int J Solids Struct* 2003;40(2):343–60.
- [86] Huang C, Subhash G, Vitton SJ. A dynamic damage growth model for uniaxial compressive response of rock aggregates. *Mech Mater* 2002;34(5):267–77.
- [87] Deshpande VS, Evans AG. Inelastic deformation and energy dissipation in ceramics: A mechanism-based constitutive model. *J Mech Phys Solids* 2008;56(10):3077–100.